Climate Dynamics (2026) 64:455
https://doi.org/10.1007/s00382-026-08402-x

ORIGINAL ARTICLE

Impact of wave coupling and the Charnock parameter on tropical circulations in a climate model

Taek-Bum Jeong[1,2] · Navajyoth Puthiyaveettil[1,2] · Joakim Kjellsson[3] · Jean-Raymond Bidlot[4] · Wonsun Park[1,2]

Received: 24 March 2026 / Accepted: 18 September 2026
© The Author(s), under exclusive licence to Springer-Verlag GmbH Germany, part of Springer Nature 2026

Abstract
Ocean surface waves play a vital role in the coupled ocean-atmosphere system by regulating the exchange of momentum and heat, yet few climate models incorporate interactive wave coupling. In this study, we examine the mean state response to coupling a wave model to an atmospheric model within a climate model. We conducted three simulations to highlight the influence of the wave model and the Charnock parameter, which controls surface roughness: a control with a constant Charnock parameter, a wave-coupled run in which the parameter responds to wave stress, and a wave-coupled model applying a modified Charnock parameterization, reducing the Charnock parameter at high wind speeds. Coupling waves reduces magnitudes of wind stress over the tropical oceans, thereby suppressing equatorial upwelling along the eastern boundaries and weakening the westward propagation of cold water. This response reduces cold sea surface temperature biases and the east–west near-surface temperature gradient bias over the tropics. In contrast, the impact of the modified Charnock parameterization is largely confined to high-latitude regions characterized by strong winds. However, when combined with wave coupling, it also contributes to a modest enhancement and spatial extension of the tropical warming signal. These processes modify large-scale overturning circulations, including a strengthening of the Hadley circulation and a weakening of the Pacific tropical and subtropical cells, resulting in an improved distribution of tropical precipitation and reduced equatorial upwelling. Our results demonstrate that incorporating sea-state-dependent momentum exchange via wave coupling can modify tropical climate features and potentially enhance the fidelity of coupled climate models.

Keywords Wave coupling · Charnock parameter · Atmosphere-ocean coupled model · Air–sea interaction · Tropical circulation

1 Introduction

Ocean surface waves play a crucial role in regulating the exchanges of momentum, heat, and gases across the air–sea interface, thereby influencing upper-ocean stratification, air–sea fluxes, and climate variability. However, many atmosphere-ocean general circulation models (AOGCMs) have historically represented wave effects only implicitly through bulk flux parameterizations, often neglecting the dependence of these exchanges on the evolving sea state as described in early theoretical frameworks (e.g., Janssen 1991). This omission has become increasingly important as atmospheric models now resolve stronger and more realistic high-wind events (Haakenstad et al. 2021), highlighting limitations in conventional roughness and drag formulations.

Brodeau et al. (2017) quantified the impacts of approximations and assumptions in bulk parameterizations on the air–sea exchange of momentum, heat, and freshwater. Their analysis showed that wind stress is highly sensitive to the formulation of the drag coefficient and largely depends on the prescribed value of the Charnock parameter. These results highlight the importance of accurately representing the Charnock parameter in bulk formulations used in climate models.

✉ Wonsun Park
wpark@pusan.ac.kr

1 Center for Climate Physics, Institute for Basic Science, Busan, South Korea

2 Department of Integrated Climate System Science, Pusan National University, Busan, South Korea

3 Rossby Centre, Swedish Meteorological and Hydrological Institute (SMHI), Norrköping, Sweden

4 European Centre for Medium-Range Weather Forecasts (ECMWF), Reading, UK

Published online: 09 October 2026

The classical Charnock relation relates the aerodynamic roughness length of the sea surface to wind stress (Charnock 1955). Wu (1980) proposed a Charnock constant of 0.018 that is consistent with the wind stress relationship across a wide range of wind conditions, from light breezes to hurricanes, and this value has since been widely adopted. However, more recent studies have shown that applying this relationship with a constant or only weakly varying coefficient can result in excessive aerodynamic drag and exaggerated wave growth under extreme wind conditions. For example, Shimura et al. (2017) demonstrated that the use of a fixed Charnock parameter larger than 0.01 leads to underestimated wind speeds in low-latitude regions dominated by weak winds, and that this limitation can be partially mitigated by reducing the drag coefficient at wind speeds below 7 m/s through the adoption of wave-dependent Charnock formulations based on wave steepness (Taylor and Yelland 2001) or wave age (Drennan et al. 2003). Observational and laboratory studies, however, consistently show that drag coefficients tend to saturate or even decrease at wind speeds above approximately 20–30 m/s (Donelan et al. 2004; Powell et al. 2003; Holthuijsen et al. 2012; Curcic and Haus 2020). Despite this, wave models that use traditional source-term formulations (Janssen 1989; Ardhuin et al. 2010) often overestimate momentum transfer during rapidly developing seas. For example, Breivik et al. (2022) showed that a reduced high-wind Charnock parameter, originally implemented in the ECMWF Integrated Forecast System (IFS) Cycle 47, can substantially mitigate biases in extreme sea states, in their wave hindcast, particularly when using high-resolution atmospheric forcing. Even in lower wind conditions, the original choice of the constant value for the Charnock parameter might not have been optimal for all ocean regions, as it is now understood that it should depend on the sea state.

These deficiencies in wave–atmosphere–ocean coupling can propagate into coupled climate systems. Atmospheric general circulation models (AGCMs), including OpenIFS, exhibit systematic wind and circulation biases linked to unresolved surface-layer processes and overly simplistic flux parameterizations (Jung et al. 2012; Roberts et al. 2019; Savita et al. 2024). Such errors distort upper-ocean mixing and circulation, sea surface temperature (SST) distribution, mid-latitude storm-track dynamics, and the variability induced by air-sea interactions, which are key drivers of climate variability. Increasing resolution or reducing time step length can partially alleviate these biases (Savita et al. 2024), but structural deficiencies in air–sea coupling due to the lack of an explicit wave representation remain underexplored.

Recent studies have demonstrated substantial progress in incorporating wave models into atmosphere-ocean general circulation models (AOGCMs), highlighting their significant effects. FIO-ESM2.0 (Bao et al. 2020), building on nonbreaking wave-induced mixing theory (Qiao et al. 2004, 2010), additionally includes Stokes drift impacts on momentum and heat fluxes, wave-induced sea spray processes, and SST diurnal-cycle parameterizations. These additions significantly reduce long-standing SST, mixed-layer depth, and El Niño/Southern Oscillation (ENSO)-related biases prevalent in the Climate Model Intercomparison Project phase 6 (CMIP6) models. Earlier studies also showed that incorporating wave-induced vertical mixing into coupled models can mitigate tropical SST biases (Song et al. 2012). Similar improvements have been demonstrated in studies integrating Langmuir turbulence (Takaya et al. 2010; Li et al. 2016; Danabasoglu et al. 2020) and advanced wave–atmosphere coupling schemes in operational forecast systems (Janssen 2004; Bidlot et al. 2020; Pineau-Guillou et al. 2020).

Despite these advances, the individual impacts of wave coupling on the coupled climate system remain difficult to isolate. Previous studies relied on atmosphere-only (Flynn and Mauritsen 2023) or atmosphere-wave coupled (Shimura et al. 2017) frameworks. Others incorporated multiple wave processes simultaneously (Bao et al. 2020). In addition, some studies relied on relatively short simulations of shorter than 100 years (Li et al. 2016, 2021), which may not be sufficient to robustly characterize the mean state response and could accordingly overstate the sensitivity of the results to the choice of Charnock parameterization. The use of regional model configurations in some of these studies further limits the extent to which the resulting circulation changes can be interpreted at the global scale. Moreover, the combined influence of surface roughness adjustments on oceanic and atmospheric circulation has not, to our knowledge, been jointly examined within a single framework. These approaches make it difficult to attribute the resulting climate responses clearly. As a result, the role of sea-state-dependent air–sea momentum exchange in the large-scale climate system remains insufficiently understood.

In this study, we address this limitation by using a fully coupled atmosphere-ocean framework with integration spanning multi-centuries. We also introduce only minimal modifications within a consistent experimental configuration. Through this approach, we examine the mean-state response of a climate model to specific sea-state-dependent modifications of the Charnock parameter while accounting for ocean feedback. Consequently, the atmospheric and oceanic responses to changes in surface roughness can be more clearly attributed. This framework also provides a basis for implementing sea-state-dependent Charnock parameter distributions in climate models. Such an approach offers a way to reduce persistent biases in climate models.

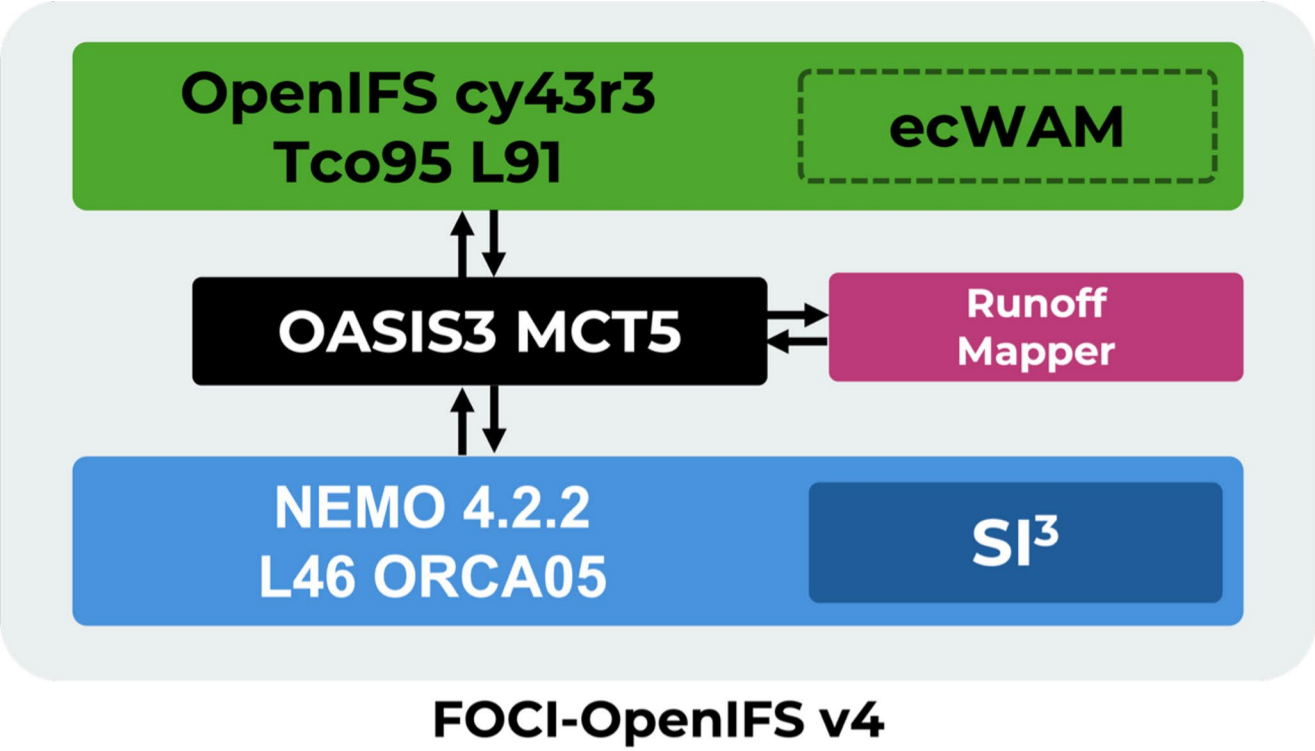


Fig. 1 Schematics of the FOCI-OpenIFS v4

Table 1 Summary of model experiments

Experiment	OpenIFS resolution	NEMO resolution	Time step	Scenario	ecWAM	Charnock modification	Model years	Total integration (years)
CTL	Tco95 L91	ORCA05 L46	OpenIFS: 30 min NEMO: 30 min	PiControl	No	No	1850–2149	300
WAM					Yes			
WAMc28						Yes		

2 Model and experiments

We employed a fully coupled atmosphere-ocean-sea ice model, Flexible Ocean and Climate Infrastructure-OpenIFS (FOCI-OpenIFS) version 4 (Sieker et al. 2026), to investigate the influence of wave-atmosphere coupling on mean climate states. In this configuration, the atmospheric component is represented by the ECMWF OpenIFS model cycle 43 release 3 (43r3; ECMWF 2017), which is coupled to the Nucleus for European Modelling of the Ocean (NEMO) version 4.2.2 (Madec and Team 2022). Atmosphere-ocean exchanges are mediated through the Ocean Atmosphere Sea Ice Soil coupler version 5 (OASIS3-MCT5; Craig et al. 2017), ensuring a physically consistent treatment of fluxes and boundary conditions across the coupled system (Fig. 1). FOCI-OpenIFS utilizes the same ocean components as FOCI (Matthes et al. 2020) but uses OpenIFS instead of ECHAM6. OpenIFS is based on the forecast model component of ECMWF Integrated Forecasting System (IFS). The code of the ECMWF wave model (ecWAM) is fully integrated with the rest of the IFS. However, it has been uncommon to use OpenIFS with ecWAM. Without the wave model, IFS reverts to using the original constant Charnock parameter that was used prior to the coupling with the wave model in 1998. It is worth noting that all subsequent IFS developments and tunings have been made with the interactive wave-atmosphere system (Janssen and Viterbo 1996; Janssen et al. 2001; Janssen 2004).

The model was integrated in a low-resolution configuration (Table 1) to assess long-term climatological responses. The atmospheric model was run at a horizontal resolution of Tco95 (triangular–cubic–octahedral grid; approximately 100 km) with 91 vertical levels, while the wave model was discretized into 24 directions (15° resolution), and 30 frequencies on a grid of 1° horizontal resolution. The ocean model employed the global tripolar ORCA05 grid (1/2°

nominal horizontal resolution) with 46 vertical levels. This configuration provides computational efficiency while retaining sufficient capability to capture large-scale atmosphere–ocean interactions relevant to the wave-coupling processes under investigation.

To highlight the influence of the wave coupling and the Charnock parameter, which controls surface roughness, we conducted three simulations: a control simulation with a constant Charnock parameter (CTL); a wave-coupled simulation in which the parameter responds to wave stress (WAM); and a wave-coupled simulation that applies a modified Charnock parameterization with Charnock reduction at high wind speeds (WAMc28). The experiments are summarized in Table 1, and details of the code configuration are provided in the subsections.

OpenIFS was initialized with CMIP6 initial conditions and forced with pre-industrial boundary conditions, e.g., constant greenhouse gas concentrations. NEMO was initialized using the World Ocean Atlas 1998 (WOA98), and the coupled model was integrated for a total of 300 years (Table 1).

2.1 Wave coupling (WAM)

In the coupled framework that explicitly represents wave components, the air-side stress (τ_a) in windy conditions (ECMWF 2017) is primarily governed by the aerodynamic roughness of the ocean surface and is thus directly determined by the roughness length (z_0). The roughness length consists of two components, namely a viscosity term for low-wind conditions following Miller et al. (1992) and a Charnock relation representing aerodynamic roughness length (Charnock 1955). These terms link surface roughness to the local wind stress and provide a physically consistent representation of momentum transfer across the air–sea interface:

$$z_0 = 0.11\frac{\nu}{u_*} + \alpha\frac{{u_*}^2}{g},$$

where α denotes the Charnock parameter, ν ($=1.5\times10^{-5}$ m^2/s) is the kinematic viscosity, u_* is the friction velocity, and g represents the gravitational acceleration. In a default configuration of OpenIFS, α is prescribed as a constant value of 0.018, which serves as a control simulation in this study (CTL). In contrast to the CTL experiment, other frameworks follow the formulation of Janssen (1989, 1991), in which the Charnock parameter is treated as a sea-state-dependent quantity. Accordingly, is expressed as

$$\alpha = \frac{\hat{\alpha}}{\sqrt{1-\frac{\tau_w}{\tau}}},$$

where τ_w represents the wave-induced momentum flux, commonly referred to as the gravity-wave or "wave stress" contribution, representing the momentum flux used to generate waves, τ is the total stress, and $\hat{\alpha}$ is a constant set to 0.006. This formulation introduces nonlinear feedback between the atmospheric wind stress and wave growth and becomes particularly important under strong wind conditions, where the aerodynamic drag could otherwise be overestimated. For all processes, relative wind speeds, defined as the wind speed relative to the ocean surface (i.e., wind speed minus ocean current velocity), were used.

In the experiment with the wave component activated (WAM), the wave model, ecWAM (ECMWF 2017), is directly coupled only to OpenIFS (Fig. 2). Wave fields, including Stokes drift and non-breaking wave contributions, are computed within ecWAM, but their influence on the ocean model occurs indirectly through modifications to the surface momentum and heat flux terms rather than through direct coupling pathways. Takaya et al. (2010) demonstrated that implementing a revised cool-skin layer scheme incorporating Langmuir circulation improves the representation of the diurnal SST amplitude. Our configuration allows wave-dependent processes to affect the air–sea momentum exchange while keeping the dynamical ocean response mediated through the atmosphere-ocean flux interface.

The WAM experiment requires more computing time than the CTL experiment because it activates and interacts with the wave model. In our high-performance computing system (Table 2), the overhead was 25%, which was not trivial. However, in IFS, the overall cost of the wave component was usually below 10%. The increase in computing time may depend on factors such as the input/output (I/O) performance of the high-performance computing (HPC) system. Information on central processing unit (CPU) usage allocation is summarized in Table 3.

2.2 A modified Charnock parameterization (WAMc28)

Before cycle 47r1, the IFS exhibited a critical limitation in representing high wind speeds under extreme weather conditions. As described in Sect. 2.1, the wave-dependent Charnock formulation could yield excessively large values under strong wind forcing, leading to an overestimation of surface roughness. Powell et al. (2003) showed that the drag coefficient starts to decrease at wind speeds exceeding 33 m/s, and Donelan et al. (2004) called it "saturation". In cycle 47r1 of the IFS, a modified Charnock parameterization that reduces the Charnock parameter at high wind speeds was introduced, which improved the relationship between maximum wind speed and minimum mean sea level pressure in intense tropical cyclones (Bidlot et al. 2020).

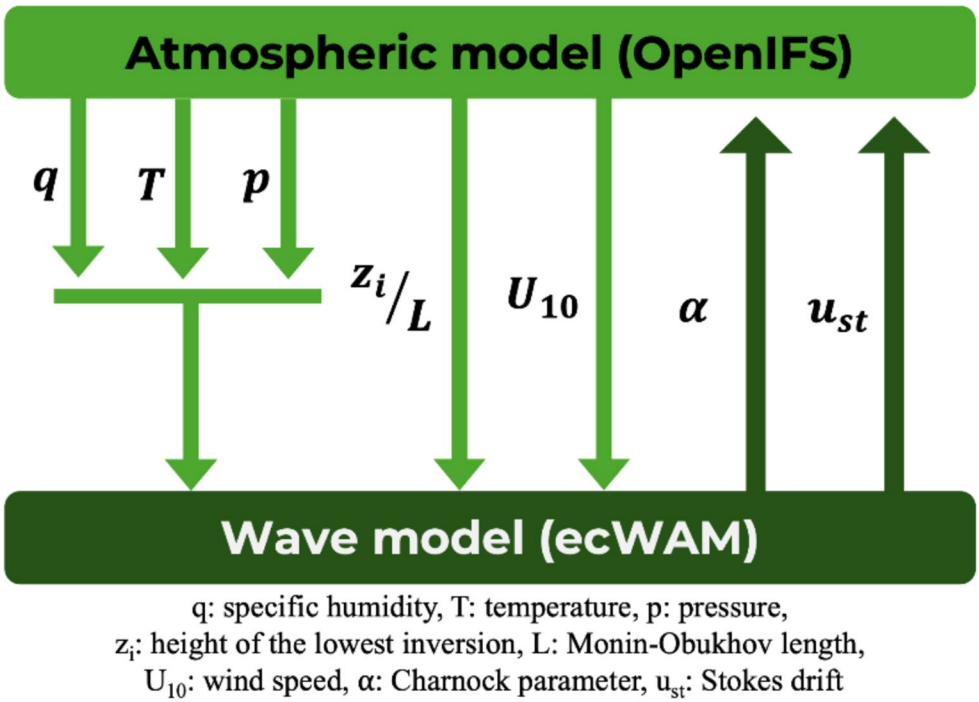


Fig. 2 Schematics of the interface between OpenIFS and ecWAM

Table 2 Configuration of the high-performance computing (HPC) resource

System	CPU	Memory per node	Peak performance
Olaf	Intel Xeon Platinum 8360Y (2.6 GHz, 36Cores)	256	1161 TF

Table 3 Comparison of CPU usage and CPU time per simulated year across experiments

Experiment	OpenIFS	NEMO	Runoff mapper (rnfmap)	IO (xios)	CPU time
CTL	432	432	1	1	45 min per year
WAM WAMc28					56 min per year

In the present study, we incorporated the modified Charnock parameterization by patching the relevant OpenIFS cy47r1 code into our model framework with cy43r3 (ECMWF 2020). This facilitates the fair assessment of the impact of the modified Charnock parameterization. While the original implementation applies the Charnock reduction at a wind speed exceeding 33 m/s, we adjusted the threshold to 28 m/s to better match our low-resolution atmosphere configuration. It is also in line with what was used by Li et al. (2021).

$$\hat{\alpha} = \hat{\alpha}_{min} + 0.5\,(\hat{\alpha}_0 - \hat{\alpha}_{min})\,[1 - \tanh\,(U_{10} - 28)]$$

$\hat{\alpha}_0 = 0.0060,\ \hat{\alpha}_{min} = 0.0001$

The parameter $\hat{\alpha}_0$ corresponds to lower wind conditions as in WAM, while $\hat{\alpha}_{min}$ is introduced as a lower bound to prevent the Charnock parameter from vanishing.

2.3 Reanalysis data

Three reanalysis datasets are employed to evaluate the model simulations. Sea surface temperature data are obtained from HadISST version 1 (Rayner et al. 2003), covering the period 1870–2014. In addition, atmospheric and vertical oceanic fields are derived from the ERA5 reanalysis (Hersbach et al. 2020) and the Ocean Reanalysis System 5 (ORAS5; Zuo et al. 2019), both spanning the period 1981–2010. It is noteworthy that the forcing fields for ORAS5 are derived from the atmospheric reanalysis ERA-Interim (Dee et al. 2011) up to 2015 and from the ECMWF operational Numerical Weather Prediction (NWP) system thereafter (Zuo et al. 2019). Accordingly, wind stress in ORAS5 is treated as a surface forcing on the ocean, rather than as an actual prognostic oceanic quantity. In this study, differences from ORAS5 are regarded as model biases. It should further be noted that cloud fractions in ERA5 are a diagnosed, rather than directly assimilated, quantity, and that ERA5 shares the same underlying IFS model physics as OpenIFS. Nonetheless, ERA5 cloud fields have shown reasonably good performance against independent observations in previous evaluations (e.g., Yao et al. 2020), and are

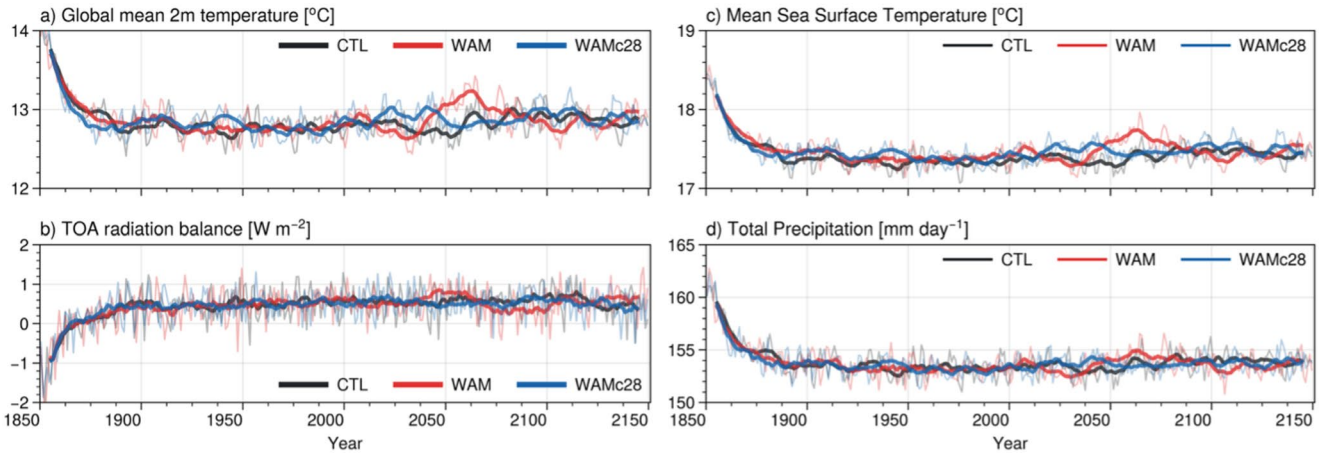


Fig. 3 Time series of annual global mean **a** 2-m surface air temperature (SAT; °C), **b** Top-of-Atmosphere radiation balance (W/m^2), **c** sea surface temperature (SST; °C) and **d** total precipitation (mm/day) for CTL (black), WAM (red), and WAMc28 (blue) simulations, respectively. The thick lines indicate the 11-year running mean time series

Table 4 Summary of global mean surface air temperature (SAT) for CMIP6 models with pre-industrial conditions

No.	Model	Mean SAT (°C)
1	FOCI-OpenIFS	12.8
2	KIOST-ESM	12.7
3	GFDL-CM4	12.7
4	FIO-ESM-2-0	13.4
5	GFDL-ESM4	13.4
6	CMCC-ESM2	13.7
7	EC-Earth3	13.8
8	MRI-ESM2-0	13.9
9	CESM2	14.0
10	MIROC6	15.2

therefore used here for consistency with the other reanalysis fields employed in this study.

3 Results

3.1 Global mean state and its response to wave coupling and Charnock parameterization

We first evaluate the overall performance and stability of the simulations under pre-industrial conditions. The global mean 2-m surface air temperature (SAT) initially exhibited a value of 14.2 °C, after which it underwent a relatively rapid decline to ~12.8 °C (Fig. 3a). While the global mean SAT may appear excessively cold, a comparison with CMIP6 models under pre-industrial conditions shows that our model lies approximately 1 °C below the multi-model mean, a departure that remains within the range of the CMIP6 ensemble (Table 4). The TOA balance reached and stabilized at about 0.5 W/m^2 at the end of the simulations (Fig. 3b), indicating quasi-equilibrium with stabilized SAT. Consistent with the SAT evolution, the global mean sea surface temperature (SST) also decreased from an initial value of 18.5 °C to around 17.4 °C (Fig. 3c). Furthermore, the total precipitation, expressed as globally integrated precipitation, showed a similar downward adjustment, decreasing from 162 mm/day to 153 mm/day (Fig. 3d). All three experiments undergo pronounced transient adjustments during the initial 50 years associated with model spin-up; therefore, the final 250 years of each simulation are used to assess the mean climate states.

We analyze the spatial distribution of the Charnock parameter averaged over the analysis period to further examine the role of wave coupling and the modified Charnock parameterization (Fig. 4a, b). In the wave-coupled experiments, the Charnock parameter generally exhibits lower values than the constant value of 0.018 prescribed in the CTL simulation. The decrease of the Charnock parameter is most pronounced in the tropics, where the Charnock parameter falls to approximately 0.012 and locally falls below 0.010 in equatorial regions. These values are comparable to those suggested by the TOGA (Tropical Ocean Global Atmosphere) COARE (Coupled Ocean–Atmosphere Response Experiment) 3.0 bulk parameterization (Fig. 4d; Fairall et al. 2003), which estimates a Charnock parameter of approximately 0.011 for relatively weak wind speeds (< 10 m/s) based on moored buoy observations in the equatorial Pacific. The relatively low Charnock parameter values simulated in the tropics imply reduced aerodynamic drag at the ocean surface. Consequently, surface wind stress decreases while surface wind speeds become slightly stronger. This relationship helps explain the tropical wind stress responses described above and provides a useful framework for interpreting the regional climate responses discussed in the following results.

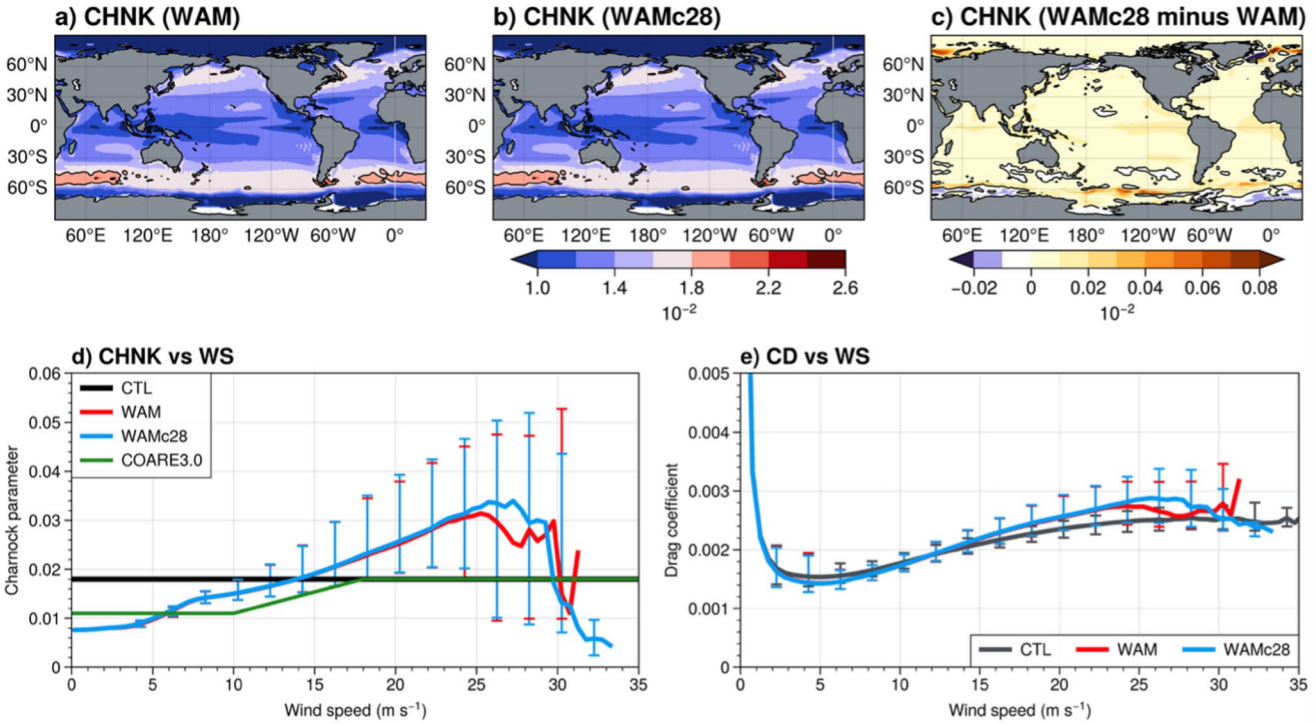


Fig. 4 **a**–**b** Climatological annual mean Charnock parameter from WAM (**a**) and WAMc28 (**b**). The bluish (reddish) color represents a Charnock parameter lower (higher) than 0.018, a constant value used in CTL. **c** Charnock parameter response to modified Charnock parameterization (WAMc28 minus WAM). The model simulations are averaged for 250 years after skipping the initial 50 years. **d** Hourly Charnock parameter as a function of 10 m wind speed and **e** drag coefficient as a function of 10 m wind speed, derived from the first year of the CTL, WAM, and WAMc28 simulations. Solid lines indicate the median value, and vertical bars represent the interquartile range (25th–75th percentiles)

The Charnock parameter increases with latitude, reaching its highest values in the mid-latitude regions of both hemispheres (45°–60°). In particular, values exceeding 0.020 are found over the Antarctic Circumpolar Current (ACC) region, where strong, persistent winds and energetic wave conditions prevail. However, applying the modified Charnock parameterization (WAMc28) results in a slight decrease in Charnock parameters over the ACC region (Fig. 4c–e).

This behavior is more clearly evident in the hourly analysis. In WAM, Charnock decreases for wind speeds exceeding 25 m/s; however, because the original parameterization does not include an upper wind-speed threshold that sustains this reduction, the decrease ceases above 28 m/s, allowing the drag coefficient to continue increasing at higher wind speeds. In WAMc28, the modified formulation introduces such an upper threshold at 28 m/s, so that a robust decreasing trend in roughness persists beyond this wind speed. As a result, wind speeds reach up to 34 m/s in WAMc28, compared with a maximum of 32 m/s in WAM (Fig. 4d–e).

The control simulation (CTL) reproduces the main features of the global SST distribution when compared with observations from the HadISST dataset spanning from 1870 to 2004. This includes a maximum SST of approximately 30.5 °C over the western equatorial Pacific (Fig. 5a, b). However, it also shows general SST biases that many coupled climate models show (Cai et al. 2021). Large cold biases of overall 3 °C with a maximum 4.7 °C occurs over the eastern and central equatorial Pacific (Fig. 5c). Conversely, a pronounced warm bias of up to 7.4 °C is present in the Kuroshio region. In addition, relatively weak warm SST biases of around 2.0 °C are observed in several regions, including the Gulf Stream, the eastern equatorial Atlantic, the Labrador Sea, and the Gulf of California. The model exhibits an overall cold SST bias, with particularly strong cold biases over the eastern North Pacific, the Southern Hemisphere oceans, and the North Atlantic. Notably, the largest cold bias, reaching approximately 7.1 °C, occurs in the North Atlantic. These results highlight the regional characteristics of SST biases in the model, which are similar to those of many climate models.

An analysis of the SST responses across the experiments indicates that, overall, the WAM and WAMc28 simulations exhibit comparable performance in global means, as shown in Fig. 3. However, there are distinct regional differences in SST biases. WAM simulation, including the interactive

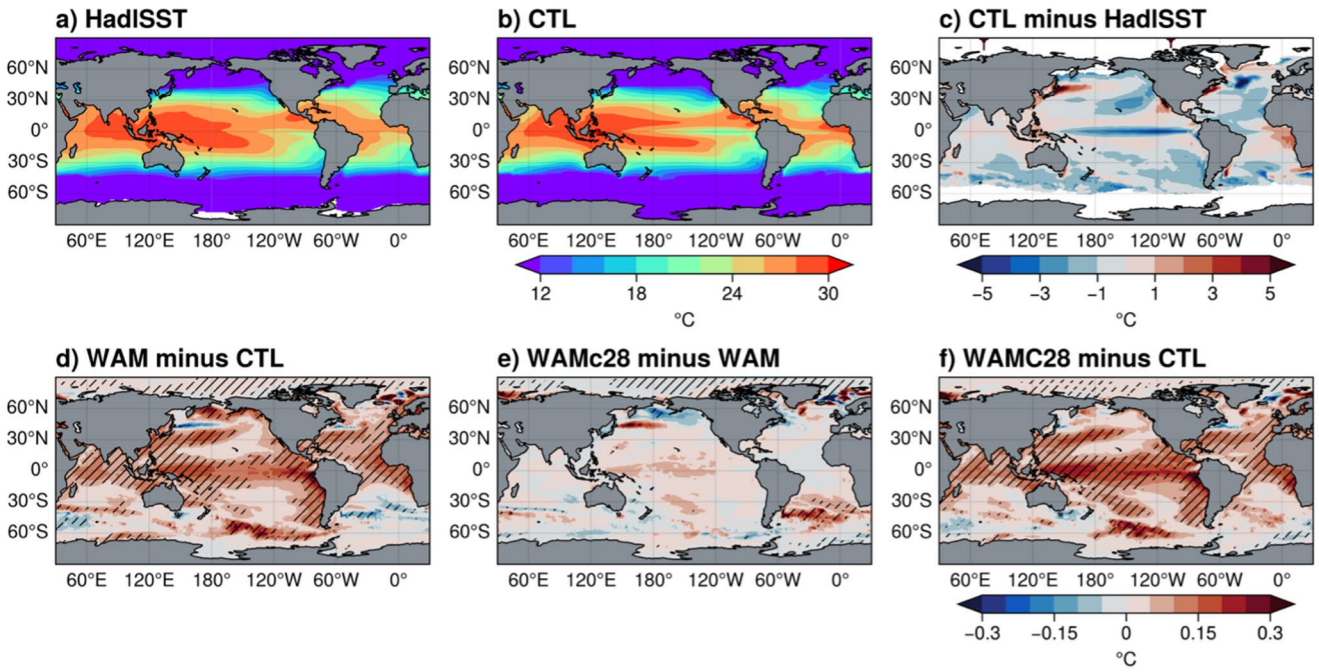


Fig. 5 **a**–**b** Climatological annual mean SSTs (°C) from HadISST (**a**) and CTL (**b**). **c** SST difference (°C) between CTL and HadISST. **d**–**f** SST responses to wave coupling (**d**; WAM minus CTL), modified Charnock parameterization (**e**; WAMc28 minus WAM), and wave coupling + modified Charnock parameterization (**f**; WAMc28 minus CTL). HadISST data are averaged from 1870 to 2004, and the model simulations for 250 years after skipping the initial 50 years. Hatching represents statistically significant points at 95% confidence level with a t-test for (**d**–**f**)

wave model ecWAM, shows a general warming tendency compared to the CTL simulation (Fig. 5d). SST increases exceeding 0.2 °C are primarily found in the equatorial Pacific, western boundary current regions, and the equatorial Atlantic and Indian Oceans. Among these regions, the most pronounced warming occurs in upwelling zones along the equatorial Pacific and Atlantic. These responses are associated with wind stress adjustments under wave coupling as described later.

When combined with wave coupling, this warming contributes to an expansion of regions exhibiting SST increases in the equatorial Pacific (Fig. 5f). Such changes facilitate the propagation of warm SST over mid-latitude regions toward the Southern Ocean (Fig. 5d). This warming is primarily attributed to reduced vertical entrainment associated with the suppressed surface wind stress, together with the advection of warmed equatorial SST via the western boundary current extension into the mid-latitudes. A broadly analogous pattern was reported by Luo et al. (2005), who found that coupling the ocean surface current to the wind stress calculation weakened the relative wind speed in the Tropics and thereby altered the basin-wide SST distribution. Over the Antarctic region, the warming is further modulated by changes in the westerlies over the ACC; the weakened westerlies in the Pacific basin suppress the equatorward propagation of cold water upwelled near 60°S, consistent with the wind stress changes shown in Fig. 6d–f. It is also supported by Webb and de Cuevas (2007), who showed, through ocean model experiments, that a small increase of wind stress (0.01 N/m^2) can increase the Ekman transport and the strength of ACC, a response consistent with the reverse mechanism proposed here for weakened westerlies.

The impact of applying a modified Charnock parameterization is relatively weak compared to that of wave coupling (Fig. 5e). Overall, only a modest warming of less than 0.1 °C is observed. Slight warming tendencies are found in the Kuroshio region. Notably, in the South Atlantic, a modified Charnock parameterization adjusts the cold bias present in the CTL simulation by approximately 10%. In addition, although not statistically significant, a weak warming of under 0.1 °C appears in the central equatorial Pacific. The warming pattern found in the Pacific is broadly consistent with previous studies (e.g., Su et al. 2018), which identified a weakening of the trade winds associated with subtropical Pacific SST anomalies. In the present study, the modified Charnock parameterization produces a comparable, albeit weak, warming through an intensification of the subtropical gyre; although this warming remains weak, it is supported by a corresponding reduction in trade wind stress (Fig. 6e–f). When combined with wave coupling, this warming contributes to an expansion of regions exhibiting SST increases in the equatorial Pacific (Fig. 5f).

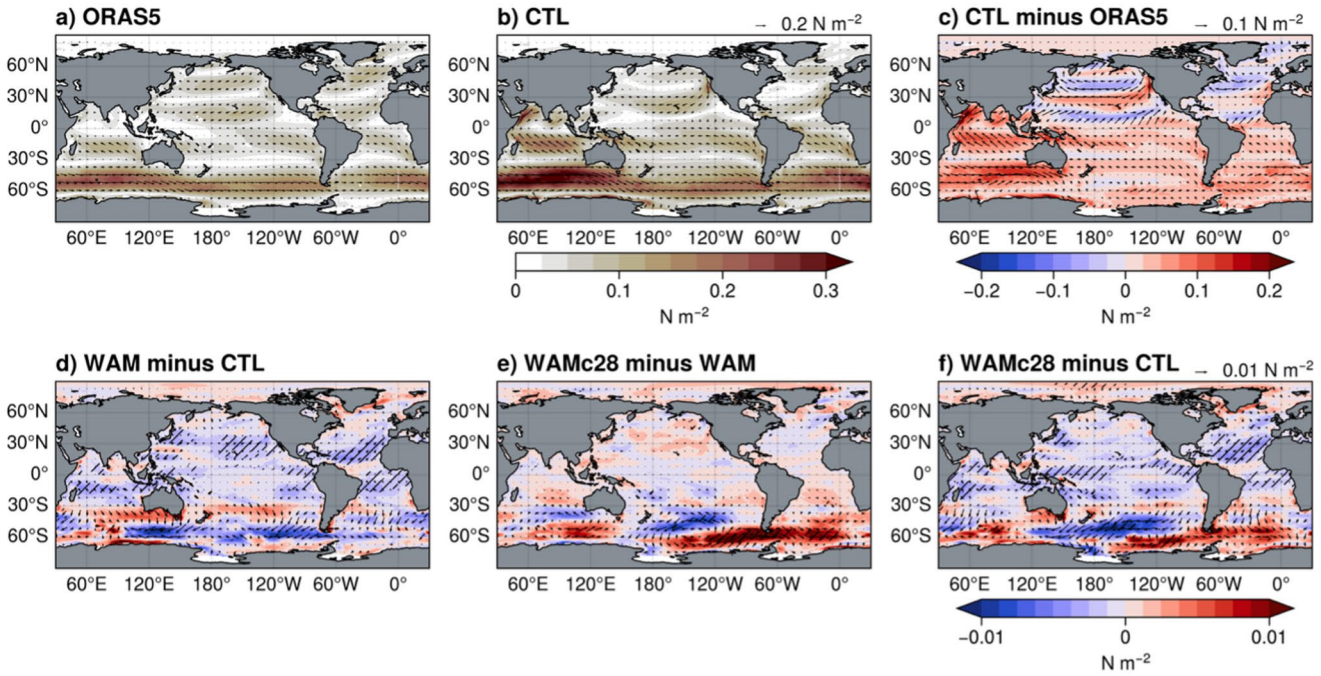


Fig. 6 **a**–**b** Climatological annual mean surface wind stress (vector) and its magnitude (N/m^2) from ORAS5 (**a**) and CTL (**b**). **c** SST difference (°C) between CTL and ORAS5. **d**–**f** Wind stress responses to wave coupling (**d**; WAM minus CTL), modified Charnock parameterization (**e**; WAMc28 minus WAM), and wave coupling + modified Charnock parameterization (**f**; WAMc28 minus CTL). ORAS5 data are averaged from 1981 to 2010, and the model simulations for 250 years after skipping the initial 50 years. Hatching represents statistically significant points at 95% confidence level with a t-test for (**d**–**f**)

Associated with this reduction in tropical Pacific cold bias, tropical Pacific SST variability is also affected. FOCI-OpenIFS exhibits higher SST variability than HadISST in the CTL simulation (Fig. S1a), and this overestimation is somewhat reduced under wave coupling and the modified Charnock parameterization. A similar tendency is found in the Niño3 SST power spectra, where the reduction relative to CTL is most evident at 4–6-year periods, the core interannual band of ENSO variability, with WAMc28 showing the closest agreement with HadISST among the three simulations (Fig. S1b).

In the CTL simulation, magnitudes of downward surface wind stress are overestimated compared to ORAS5 (Fig. 6a–c). Across the tropical oceans, applying a spatially varying Charnock parameter due to implementation of ecWAM results in a weakening of surface wind stress up to 0.002 N/m^2 (Fig. 6d). As a result, upwelling along the eastern boundaries is reduced, and the westward propagation of cold water from the cold tongue region is suppressed. The magnitude of the wind stress reduction increases with latitude, reaching up to 0.003 N/m^2 in mid-latitude regions. This weakening extends into the subtropical regions, leading to a reduced wind-driven circulation, and particularly affects Ekman transport in low-latitude regions where wind speeds are relatively weak.

The application of a modified Charnock parameterization produces enhanced wind stress in high-latitude regions, including the Drake Passage (Fig. 6e), indicating that the Charnock reduction scheme exerts a stronger influence under high-wind conditions. This response reflects a decrease in surface roughness under Charnock reduction, which enhances near-surface wind speeds and ultimately increases the wind stress. Although a reduction in the Charnock parameter directly decreases the drag coefficient, the accompanying increase in near-surface wind speed—since wind stress scales with the square of wind speed—can outweigh this direct effect, resulting in a net enhancement of wind stress under high-wind conditions (Fig. 4e). Strengthened westerly wind stress over the ACC region leads to an increase in ACC transport, with the WAMc28 experiment exhibiting transports approximately 5 Sv stronger than those in the other two experiments with mean values of about 130 Sv (not shown).

Overall, these results reveal a clear spatial separation in the dominant mechanisms governing wind stress responses. Wave coupling dominates across much of the low- and mid-latitude oceans, where it modulates wind stress in close association with changes in vertical mixing and the global-scale overturning circulation—consistent with the tropical wind stress weakening described above, which drives reduced equatorial upwelling and a suppressed cold tongue.

In contrast, the influence of a modified Charnock parameterization becomes increasingly prominent toward higher latitudes, particularly in the Southern Hemisphere, where it predominantly affects large-scale horizontal circulation under high-wind conditions. Together, these processes lead to a reduction in surface momentum fluxes over the tropics, thereby weakening equatorial upwelling, reducing cold SST biases.

3.2 Response of tropical circulation

As shown above, the SST response to wave coupling is concentrated primarily in the tropics. This section focuses on this response in the tropics and provides a detailed examination of the associated physical mechanisms. We further assess the influence of wave coupling on ocean circulation by analyzing the near-surface and subsurface vertical structure as well as the overturning circulation.

Table 5 summarizes the global and tropical mean bias and RMSE of SST, precipitation, and wind stress for each simulation. Wave coupling reduces the global and tropical mean SST bias relative to CTL, with the largest reduction found in the tropics (from −0.51 to −0.41/−0.42 °C). A comparable reduction is found in wind stress bias, particularly in the tropics, where the mean bias decreases by more than 0.001 N/m^2 under WAM and WAMc28 relative to CTL. The change in precipitation bias is comparatively small relative to these two variables.

To investigate the relationship between SST responses and changes in surface wind stress in the tropics due to the inclusion of the wave model, we analyzed the mean seasonal cycle of differences in zonally averaged SST and zonal wind stress along the equatorial band (5° S–5° N; Fig. 7).

The observed monthly SST evolution exhibits a pronounced annual cycle in the eastern equatorial Pacific (Fig. 7a). SSTs in the western equatorial Pacific display relatively weak variability and remain above 29.0 °C throughout the year, whereas the eastern equatorial Pacific shows much stronger seasonal variability. In the eastern equatorial Pacific, SSTs peak at approximately 27.0 °C during boreal spring (March–May) and reach a minimum of around 23.0 °C in boreal autumn (September–November). In the equatorial Indian Ocean, SSTs remain above 28.0 °C throughout the year with little seasonal dependence. The Atlantic Ocean exhibits a seasonal cycle similar to that of the eastern Pacific, but with SSTs that are approximately 1.0 °C warmer. The CTL simulation exhibits a pronounced cold bias exceeding 5.0 °C over the eastern equatorial Pacific during early boreal summer (June–July), accompanied by an overestimation of zonal wind stress associated with strengthened trade winds and enhanced low-level cloud cover (Fig. 7b, e, h).

When the wave model is included, an approximately 0.2 °C basin-wide tropical SST warming, with a maximum of 0.5 °C, is evident (Fig. 7c). A pronounced SST signal emerges over the eastern equatorial Pacific during boreal spring (April–June), coincident with a weakening of the anomalously strong easterly wind stress present in CTL (Fig. 7f) and the associated reduction in equatorial upwelling, which we interpret as the primary driver of this warming. This dynamically driven SST increase is further reinforced by a concurrent reduction in low-level cloud cover (Fig. 7i): because low-level clouds preferentially form over relatively cool SSTs and have high albedo, their reduction increases the shortwave flux reaching the surface, providing a secondary radiative feedback that amplifies the initial warming on short time scales (Kim et al. 2022).

To further examine this mechanism, we analyzed the monthly evolution of SST, wind stress, upwelling, cloud cover, and surface heat fluxes separately for the Niño 1+2 and Niño 3 regions (Figs. S2, S3). In both regions, the April SST peak is primarily driven by weakened wind stress and reduced Ekman upwelling. The two regions differ, however, in their subsequent cloud response. In Niño 1+2, the SST rise coincides with increased precipitation and increased mid- and high-level cloud cover, while the net surface heat flux remains strongly negative through this period (Fig. S3g–h), indicating that the enhanced cloudiness is a byproduct of convection rather than a radiative driver of the warming. In Niño 3, precipitation increases only modestly, while low-level cloud cover decreases gradually from spring onward, accompanied by a shift of the net heat flux to positive values (Fig. S2d, g, h)—consistent with the low-cloud feedback described above acting to sustain, rather than initiate, the warming.

These seasonal patterns indicate that the timing and location of SST responses are primarily set by changes in wind stress and upwelling, with cloud-radiative feedback acting as an amplifying rather than an initiating mechanism. This distinction—between a dynamically driven initial response and a radiatively reinforced secondary feedback—is consistent with the broader literature on eastern tropical SST

Table 5 Summary of mean bias and root-mean-square error (RMSE) of sea surface temperature (SST), precipitation, and wind stress over the global ocean and tropical ocean (25° S–25° N) in each simulation

Variable	Exp	Global	Tropics
SST (°C)	CTL	−0.74 (1.34)	−0.51 (1.11)
	WAM	−0.68 (1.31)	−0.42 (1.07)
	WAMc28	−0.67 (1.30)	−0.41 (1.07)
Precipitation (mm day^{-1})	CTL	0.04 (1.37)	0.28 (1.88)
	WAM	0.04 (1.36)	0.27 (1.87)
	WAMc28	0.04 (1.36)	0.27 (1.87)
Wind stress (10^{-3} N m^{-2})	CTL	2.87 (12.17)	3.38 (11.00)
	WAM	2.42 (12.26)	2.07 (10.61)
	WAMc28	2.38 (12.27)	1.98 (10.61)

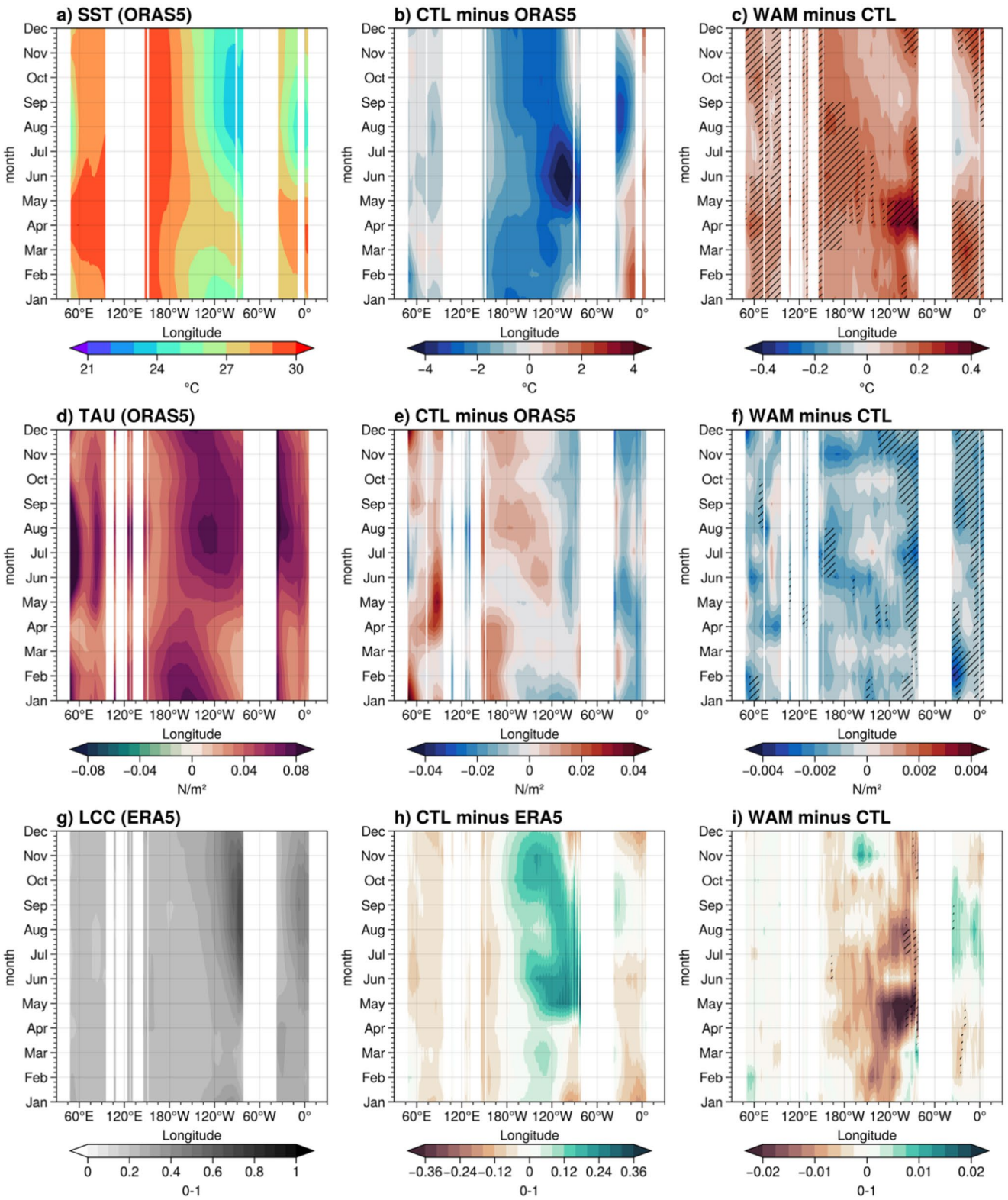


Fig. 7 **a**, **d**, **g** Seasonal cycles of SST (**a**; °C), magnitude of wind stress (**d**; N/m^2) from ORAS5, and low-level cloud (**g**; 0–1) from ERA5, and **b**, **e**, **f** corresponding differences between CTL and ECMWF datasets along the equator (5° S–5° N). **c**, **f**, **i** Responses of the corresponding variables to wave coupling (WAM minus CTL). ORAS5 and ERA5 data are averaged over 1981–2010, and the model simulations for 250 years after skipping the initial 50 years. Hatching represents statistically significant points at the 95% confidence level with a t-test for (**c**, **f**, **i**)

biases, which similarly identifies reduced low-cloud cover as a source of enhanced shortwave absorption, though there implicated as a structural driver of the mean warm bias rather than a secondary amplifier (Zuidema et al. 2016). While the SST response is statistically significant at the 95% confidence level across broader seasons and longitudes, statistically significant differences in zonal wind stress and low-level cloud cover are limited to the eastern equatorial Pacific (Fig. 7c, f, i), consistent with wind stress change being the more spatially confined but primary driver of the SST response.

Changes in wind stress and surface fluxes influence not only the surface ocean but also the vertical structure of the tropical ocean. An analysis of the vertical structure is therefore essential for assessing the model representation of ocean heat content and subsurface mixing. Examining the vertical structure of potential temperature along the equator, the observations exhibit gentle west-to-east gradients (Fig. 8a), whereas the CTL simulation shows a markedly steeper slope (Fig. 8b). Excessively strong upwelling near the eastern boundary lifts cold water, leading to a pronounced subsurface cold bias exceeding 5.0 °C within the upper 100 m. Conversely, upwelling is not adequately simulated near the western boundary, resulting in a weak subsurface warm bias in that region (Fig. 8b–c). Similar subsurface cold biases are also evident in the equatorial Indian and Atlantic Oceans, with the strongest cold bias occurring in the subsurface equatorial Atlantic. Overall, these biases are related to the overestimated wind stress associated with trade winds in the CTL experiment.

In the WAM experiment, the cold biases found near the surface in the western boundary regions and in the subsurface layers near the eastern boundary are partially resolved (Fig. 8d). When the wave model is coupled, reductions in surface wind stress led to weaker vertical mixing throughout the tropical oceans (Fig. 8d). In addition, upwelling near the eastern boundaries is weakened, partially relaxing the zonal east–west temperature gradient. Similar tendencies are also observed in the Indian and Atlantic Oceans.

To better understand changes in ocean circulation, we examined how the shallow, meridional overturning circulation responds in the Indo-Pacific and Atlantic sectors (Fig. 9a, b). The tropical cell (TC) and the subtropical cell (STC) are components of the circulation. (Lohmann and Latif 2005). These cells share equatorial upwelling, which is driven by Ekman divergence and poleward surface Ekman transport. When wave coupling is included, the tropical cells in the Indo-Pacific sector weaken in both hemispheres (Fig. 9c, d), consistent with the reduced equatorial upwelling discussed above. In the Atlantic sector, a weakening of the subtropical cell is also evident, suggesting broader meridional circulation responses consistent with the reduction in low-latitude wind stress of 0.050–0.100 N/m^2 (Fig. 6), which drives a broader SST warming tendency across the Atlantic Ocean.

Returning to the vertical temperature responses, we further examine their individual contributions by wave coupling and a modified Charnock parameterization. In contrast to the strong response to wave coupling (see Fig. 8d), the impact of a modified Charnock parameterization alone is weak across all basins and remains statistically insignificant (Fig. 8e). However, when wave coupling and the modified

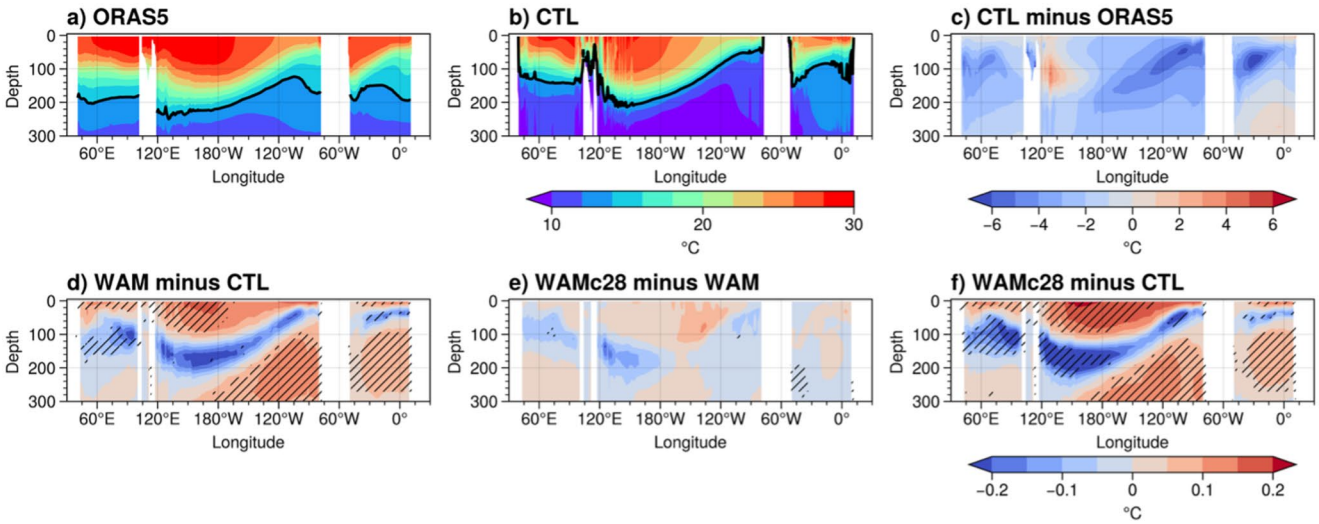


Fig. 8 **a**–**b** Vertical structures of equatorial potential temperature (°C) from ORAS5 (**a**) and CTL (**b**). Black lines indicate the depth of 14 °C isotherm. **c** Potential temperature difference (°C) between CTL and ORAS5. **d**–**f** Potential temperature responses to wave coupling (**d**; WAM minus CTL), modified Charnock parameterization (**e**; WAMc28 minus WAM), and wave coupling + modified Charnock parameterization (**f**; WAMc28 minus CTL). ORAS5 data are averaged from 1981 to 2010, and the model simulations for 250 years after skipping the initial 50 years. Hatching represents statistically significant points at the 95% confidence level with a t-test for (**d**–**f**)

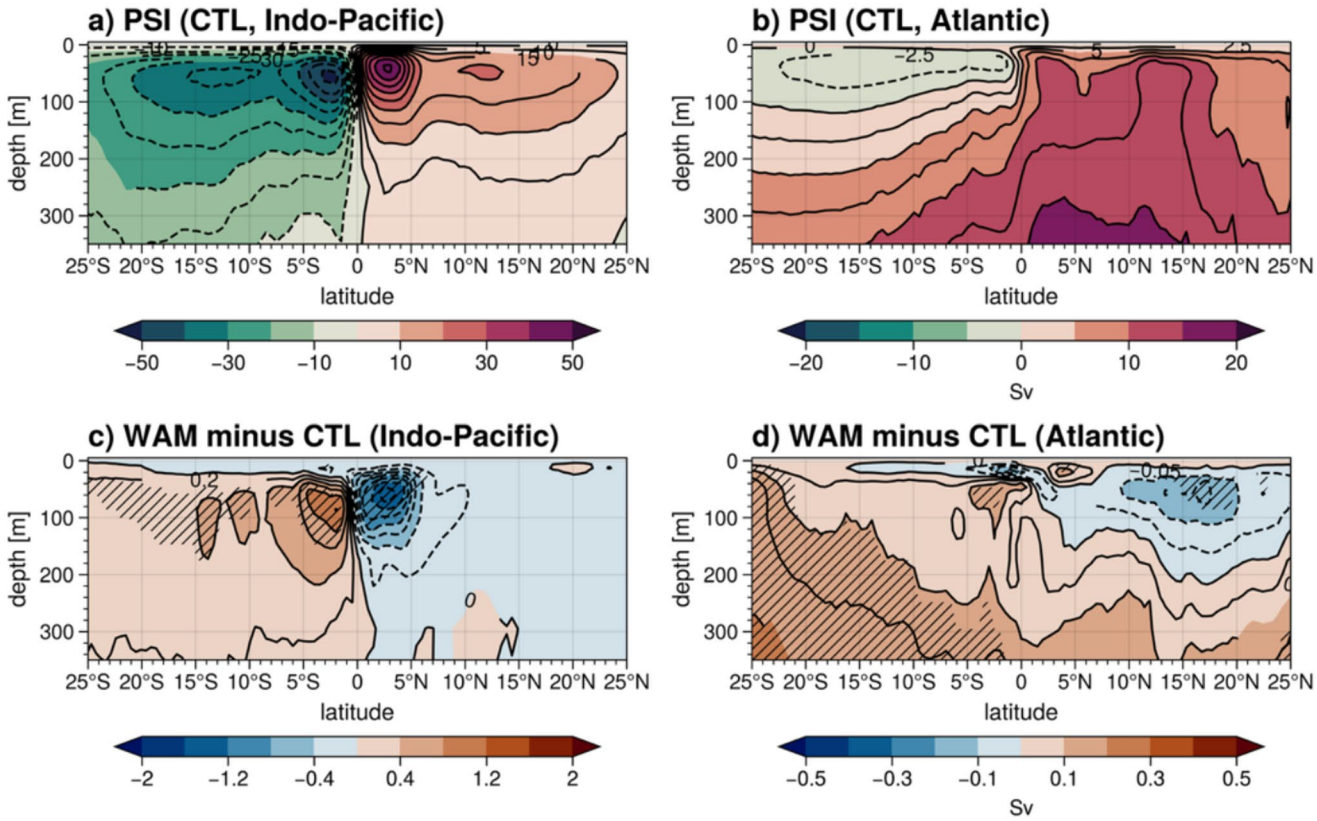


Fig. 9 **a**, **b** Climatological annual mean overturning streamfunction (Sv) over the tropical Indo-Pacific (**a**) and the tropical Atlantic (**b**) from CTL. **c**, **d** Overturning streamfunction responses to wave coupling (WAM minus CTL) over the tropical Indo-Pacific (**c**) and the tropical Atlantic (**d**). The model simulations are averaged for 250 years after skipping the initial 50 years. Hatching represents statistically significant points at the 95% confidence level with a t-test for (**c**-**d**). The contour lines are spaced at half-intervals relative to the shading

Charnock parameterization are applied simultaneously, their effect is slightly amplified (Fig. 8f), along with modest SST warming over a larger area (Fig. 5f). This suggests that applying wave-dependent Charnock parameterization and Charnock reduction simultaneously at high wind speeds creates conditions that favor warmer SSTs in tropical oceans. This highlights the complementary roles of these mechanisms in modulating surface ocean temperatures.

Wave coupling also modulates large-scale atmospheric circulation, including the Hadley circulation. To quantify the Hadley circulation response, we computed the mass streamfunction derived from the zonally averaged meridional wind, given as

$$\Psi\ (\theta\,,p) = \frac{2\pi\ a\cos\theta}{g}\int_{P}^{ps} \upsilon\,(\theta\,,p)\,dp,$$

where denotes latitude, is the Earth's radius, p is pressure, P_S is the surface pressure, is the gravitational acceleration, and is the zonally averaged meridional wind velocity (Nguyen et al. 2013; Sun 2018). This streamfunction represents the rate of meridional mass transport between a given pressure level and the top of the atmosphere at a specified latitude (Hess and Chemke 2024; Kim et al. 2017).

The Hadley circulation in the model simulations exhibits a broadly similar structure to that derived from ERA5, but notable discrepancies are evident in both its strength and spatial extent. The CTL simulation produces a weaker and more spatially broader circulation, indicating an underestimation of the overall overturning intensity relative to ERA5 (Fig. 10a–c). In particular, the bias in circulation between 15° S and 15° N implies a weakening of the ascending branch over the Intertropical Convergence Zone (ITCZ). This weakening is consistent with well-documented tropical precipitation biases in coupled climate models, including a spurious double structure, position bias, and misrepresented seasonal migration.

Following the methodology of Wang et al. (2020), the position of the Hadley circulation is diagnosed by measuring the latitude of zero crosses of the meridional mass streamfunction averaged between 400 and 600 hPa (Table 6). The CTL simulation shows an approximately 1° northward displacement of the ITCZ, defined as the central line of the meridional mass streamfunction. In addition, the boundaries of the Hadley circulation are displaced by 2.13° in the

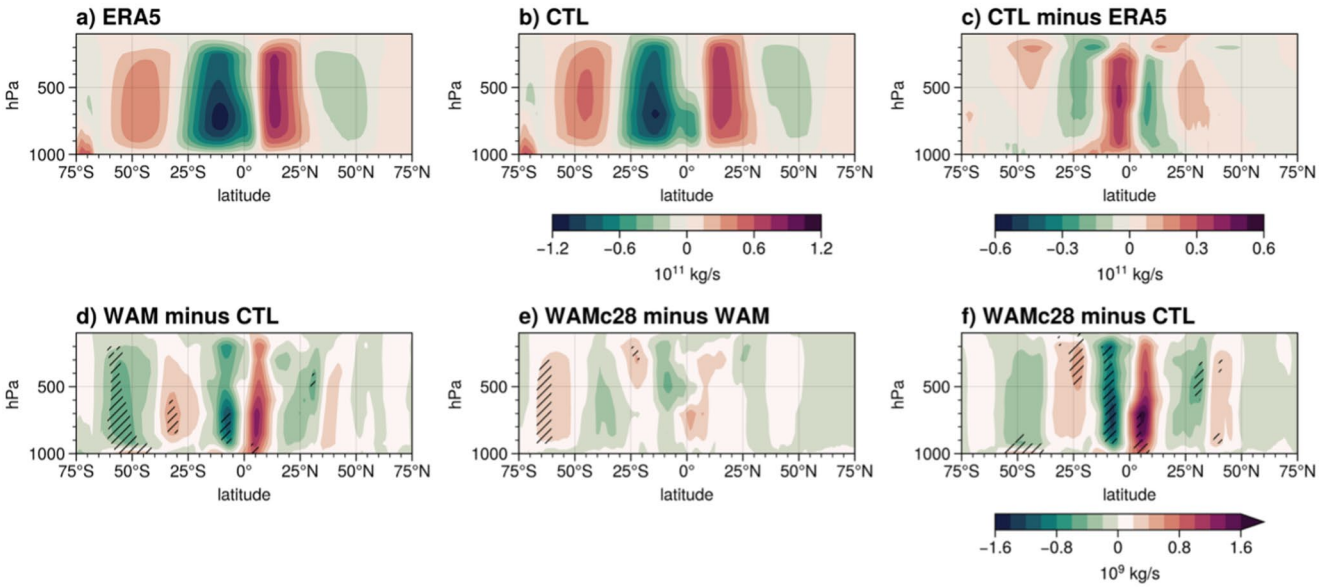


Fig. 10 **a**, **b** Climatological annual mean Hadley circulation (mass streamfunction; 10^{11} kg/s) from ERA5 (**a**) and CTL (**b**). **c** Hadley circulation difference (10^{11} kg/s) between CTL and ERA5. **d**–**f** Hadley circulation responses (10^{9} kg/s) to wave coupling (**d**; WAM minus CTL), modified Charnock parameterization (**e**; WAMc28 minus WAM), and wave coupling and modified Charnock parameterization (**f**; WAMc28 minus CTL). ERA5 data are averaged for 1981–2010, and model simulations for 250 years after skipping the initial 50 years. Hatching represents statistically significant points at the 95% confidence level with a t-test for (**d**–**f**)

Table 6 Comparison of annual mean Hadley circulation positions (values in parentheses indicate the bias compared to ERA5)

		Central line	NH	SH
Position	ERA5	4.86° N	29.14° N	30.47° S
	CTL	5.84° N (0.98)	31.27° N (2.13)	31.91° S (1.44)
	WAM	5.71° N (0.85)	31.18° N (2.04)	31.85° S (1.38)
	WAMc28	5.69° N (0.83)	31.17° N (2.03)	31.87° S (1.40)

Northern Hemisphere and 1.44° in the Southern Hemisphere relative to ERA5, indicating an overall poleward expansion of the circulation. These positional biases are accompanied by a weaker circulation strength. The maximum and minimum values of the mass streamfunction in ERA5 are 0.81×10^{11} kg/s and -1.13×10^{11} kg/s, respectively, whereas the CTL simulation yields reduced extrema of 0.71×10^{11} kg/s and -1.09×10^{11} kg/s (Fig. 10a, b).

When wave coupling is introduced, these discrepancies are partially alleviated. The positional biases of the Hadley circulation are reduced by approximately 0.1° on average, indicating a modest but systematic improvement in the representation of the circulation structure. In terms of intensity, no notable improvement is found in the extrema. However, the discrepancy in equatorial overturning strength is reduced by about 5% (Fig. 10d). This improvement is primarily associated with a strengthening and narrowing of the ascending branch, bringing the simulated circulation closer to that of ERA5.

Moreover, the influence of wave coupling is not limited to the tropics. A broader response is evident, extending from the subtropical regions to the subpolar Southern Hemisphere, suggesting that wave–atmosphere interactions modulate the large-scale overturning circulation across a wide meridional range. The impact of the modified Charnock parameterization is relatively small, with response generally remaining below 1% (Fig. 10e).

This atmospheric circulation response is also closely associated with the distribution of tropical precipitation. The tropical rain belt in the CTL simulation exhibits a characteristic double-ITCZ structure (Tian and Dong 2020; Fig. 11a–c). As a result, the model shows a pronounced contrast, with a drier bias near the equator and a wetter bias across the remaining tropical regions relative to ERA5. When wave coupling is included, however, the precipitation distribution becomes more concentrated toward the equator, with an increase of approximately 0.4 mm day^{-1} within 10° S–10° N (Fig. 11d). This equatorward concentration leads to an overall improvement in the simulated tropical precipitation distribution, although biases persist in parts of the equatorial Atlantic.

This tripolar improvement pattern is consistent with the precipitation response linked to the asymmetric structure of the second Empirical Orthogonal Function (EOF) mode of the Hadley circulation (Wang et al. 2020). Although the ITCZ shifts northward by approximately 0.1°, the precipitation pattern is primarily controlled by the enhanced

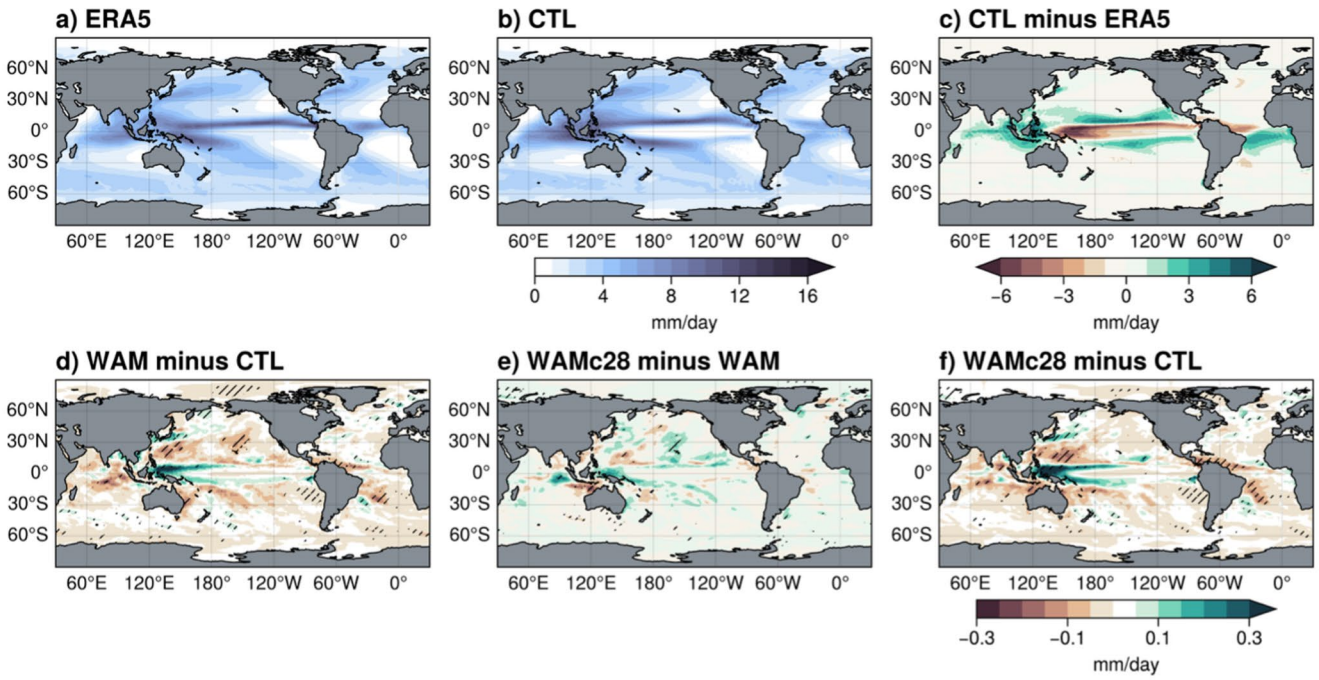


Fig. 11 **a**, **b** Climatological annual mean precipitation (mm/day) from ERA5 (**a**) and CTL (**b**). **c** Precipitation difference between CTL and ERA5 (mm/day) in CTL. **d**–**f** Precipitation responses to wave coupling (**d**; WAM minus CTL), modified Charnock parameterization (**e**; WAMc28 minus WAM), and wave coupling + modified Charnock parameterization (**f**; WAMc28 minus CTL). ERA5 data are averaged for 1981–2010, and model simulations for 250 years after skipping the initial 50 years. Hatching represents statistically significant points at the 95% confidence level with a t-test for (**d**–**f**)

asymmetry of the Hadley circulation, which is characterized by a narrower and stronger structure.

Consistent with the circulation response, the impact of the modified Charnock parameterization is generally small and does not exhibit statistically significant differences over most regions (Fig. 11e). Nevertheless, when combined with wave coupling, the inclusion of the modified parameterization contributes to an expansion of the statistically significant areas in the precipitation response (Fig. 11f). This suggests that, although its direct influence is relatively weak, the modified Charnock parameterization acts to spatially extend and amplify the wave-coupling-induced improvement in tropical precipitation distribution when applied in combination.

This behavior is consistent with previous studies examining Hadley circulation responses to prescribed wind-stress adjustments. Flynn and Mauritsen (2023), using a non-dimensional wind-stress parameter defined as the ratio of wind stress to the turbulent kinetic energy, showed that modifications in surface stress alter tropical wind speeds and thereby regulate the Hadley circulation and the associated precipitation distribution. Similarly, Shimura et al. (2017) varied the Charnock constant from 0.001 to 0.030, modifying surface stress through changes in aerodynamic roughness. Although the wind-stress adjustments differed in magnitude and sign between these studies, both reported intensified tropical trade winds accompanying the Hadley circulation response. This common enhancement of wind speed suggests that the resulting circulation and precipitation changes are more directly linked to strengthened trade winds than to the prescribed stress adjustments themselves.

Despite differences in experimental design, including the use of a fully coupled ocean–atmosphere framework and a substantially longer integration period in the present study, similar linkages among tropical wind speed variations, Hadley circulation adjustments, and precipitation redistribution are evident. In addition, a comparable but weaker pattern of tropical wind speed changes, Hadley circulation adjustments, and precipitation redistribution is found in the experiment applying the modified Charnock parameterization alone. When wave coupling and the reduction of the Charnock parameter at high wind speeds are applied simultaneously, the atmospheric response becomes stronger and more spatially extensive, as evidenced by a further mitigation of the double-ITCZ bias and a narrowing of the tropical precipitation distribution toward the equator, indicating a mutually reinforcing influence on the tropical overturning circulation. It should be noted, however, that these improvements are not spatially uniform: the wet bias is locally amplified over parts of the Maritime Continent, and the dry bias along the South American Atlantic coast is notably enhanced, both of which warrant further investigation.

4 Summary and discussion

We present the mean state change in a climate model resulting from the inclusion of an interactive wave model and a modified Charnock parameterization that reduces the Charnock parameter at wind speeds exceeding 28 m/s. Three simulations with a fully coupled atmosphere-ocean-sea ice model, the FOCI-OpenIFS, are conducted: One control simulation with a constant Charnock parameter without an interactive wave model (CTL), another a wave-coupled experiment using sea-state-dependent Charnock parameter from ecWAM (WAM), and the third experiment that applies a modified Charnock parameterization for high wind speed (WAMc28).

Incorporating sea-state-dependent surface roughness based on wave stress in ecWAM (WAM) reduces surface wind stress across the tropics by correcting the overestimated downward momentum flux in CTL. As a result, the model produces dynamically significant modifications in the upper-ocean structure and a reduction of cold SST biases through weakened trade-wind-induced drag over the equatorial Pacific. These SST responses to wave coupling are primarily governed by a weakening of Ekman upwelling associated with the reduced tropical wind stress. In particular, the Niño1+2 region exhibits enhanced convection in response to SST warming, leading to an increase in middle- to high-level cloud cover, whereas the Niño3 region shows a reduction in low cloud cover that reinforces the persistent warming through the low cloud–SST feedback. The modified Charnock parameterization (WAMc28) adopted from IFS cy47r1 exerts only a minor influence when applied alone, and its impacts remain largely confined to high latitudes. Wind speeds exceeding 25 m/s, the threshold above which the modified scheme becomes effective, occur only rarely in this region. However, when used in combination with wave coupling, the scheme broadens the warming SST response across the tropics, suggesting that a modified Charnock parameterization may influence SSTs in low-resolution climate simulations. However, we also found that the modified Charnock parameterization can amplify the pre-existing overestimation of wind stress in certain high-latitude regions. This characteristic should therefore be taken into account in future tuning efforts.

Changes in surface stress have been identified as a key variable affecting the impact of the wave model on the climate model. This leads to corresponding adjustments in oceanic and atmospheric circulation. The tropical and subtropical overturning cells weaken slightly, which is consistent with reduced meridional wind stress and diminished surface divergence. In the atmosphere, the enhanced tropical precipitation and modest strengthening of the Hadley circulation resemble the response to strengthened trade winds reported by Shimura et al. (2017). However, our analysis incorporates the ocean's dynamic response to reduced wind stress. This enables us to interpret atmospheric changes alongside the associated adjustments in ocean circulation, a process that cannot be replicated in atmosphere-only experiments. While earlier studies generally assumed that stronger trade winds lead to concurrent intensification of both upper-ocean overturning and the Hadley circulation, our analysis shows that the Charnock adjustment enables opposing responses of the two circulations.

Overall, our results suggest that explicitly modeling sea state-dependent surface stress could improve the performance of the coupled climate system to a limited extent. Specifically, representing wave-dependent air–sea momentum exchange may help to reduce SST biases. It implies that the ecWAM should be regarded as an integral component of OpenIFS, comparable to other elements of the IFS, and our results demonstrate why it should not be disabled. Moreover, in more recent versions of OpenIFS, the run-time performance of ecWAM has been substantially improved, leading to a much lower computational cost. However, several limitations remain. Using a relatively low-resolution model configuration leads to persistent cold SST biases, particularly in the equatorial Pacific. This restricts the extent to which wave coupling can improve the mean state. Notably, the residual mean state SST bias in the current configuration (up to several °C in the eastern equatorial Pacific and the North Atlantic; Fig. 5c) remains an order of magnitude larger than the SST response attributable to wave coupling (0.1–0.5 °C; Figs. 5d and 7c), indicating that sea-state-dependent surface stress addresses only one of several contributing sources of the model's mean state bias. Although the resulting improvement is therefore modest in absolute terms, quantifying this contribution is considered relevant in light of the growing interest within the climate modeling community in coupling wave models to atmosphere–ocean general circulation models.

In the current version of FOCI-OpenIFS (version 4), ecWAM operates as a component of OpenIFS but does not directly transmit wave components to NEMO; the effects of Stokes drift and non-breaking waves are coupled to the ocean only indirectly. Further model development is therefore required to fully capture the effects of wave coupling. Furthermore, as our analysis is based solely on pre-industrial simulations, the implications for historical climate variability and future projections cannot yet be fully evaluated. Additional experiments, including historical and SSP scenario simulations, and comparisons with CMIP6 models, are necessary to evaluate whether the improvements found here translate into more realistic SST patterns under changing climate conditions.

Supplementary Information The online version contains supplementary material available at https://doi.org/10.1007/s00382-026-08402-x.

Acknowledgements The simulations were conducted on the IBS supercomputer "Olaf". We also acknowledge the support of KREONET. We appreciate the comments by two reviewers that helped improve the manuscript.

Author contributions Wonsun Park conceived the study. Taek-Bum Jeong conducted the simulations with the help of Navajyoth Puthiyaveettil and Joakim Kjellsson. Joakim Kjellsson provided FOCI-OpenIFS, and Jean-Raymond Bidlot provided a modified Charnock parameterization update in OpenIFS. Taek-Bum Jeong performed the analysis and wrote the first draft of the manuscript, and all authors commented on previous versions of the manuscript. All authors read and approved the final manuscript.

Funding This work is supported by the Institute for Basic Science (IBS-R028-D1) and the Korea Institute of Marine Science and Technology Promotion (KIMST) funded by the Ministry of Oceans and Fisheries, Korea (RS-2023-00256330; 20220548, PM63990).

Data availability The data used to create the figures will be made available before publication.

Declarations

Conflict of interest The authors have no relevant financial or non-financial interests to disclose.

References

Ardhuin F, Rogers E, Babanin AV, Filipot J, Magne R, Roland A, van der Westhuysen A, Queffeulou P, Lefevre J, Aouf L, Collard F (2010) Semiempirical dissipation source functions for ocean waves. Part I: definition, calibration, and validation. J Phys Oceanogr 40:1917–1941. https://doi.org/10.1175/2010JPO4324.1

Bao Y, Song Z, Qiao F (2020) FIO-ESM version 2.0: model description and evaluation. J Geophys Res-Oceans 125: e2019JC016036 https://doi.org/10.1029/2019JC016036

Bidlot JR, Prates F, Ribas R, Mueller-Quintino A, Crepulja M, Vitart F (2020) Enhancing tropical cyclone wind forecasts. ECMWF Newsl 164:33–37. https://doi.org/10.21957/k0w4fp581h

Breivik Ø, Carrasco A, Haakenstad H, Aarnes OJ, Behrens A, Bidlot J-R, Björkqvist J-V, Bohlinger P, Furevik BR, Staneva J, Reistad M (2022) The impact of a reduced high-wind charnock parameter on wave growth with application to the north sea, the Norwegian Sea, and the Arctic Ocean. J Geophys Res-Oceans 127:e2021JC018196 https://doi.org/10.1029/2021JC018196

Brodeau L, Barnier B, Gulev SK, Woods C (2017) Climatologically significant effects of some approximations in the bulk parameterizations of turbulent air–sea fluxes. J Phys Oceanogr 47(1):5–28. https://doi.org/10.1175/JPO-D-16-0169.1

Cai W, Santoso A, Collins M, Dewitte B, Karamperidou C, Kug J-S, Lengaigne M, McPhaden MJ, Stuecker MF, Taschetto AS, Timmermann A, Wu L, Yeh S-W, Wang G, Ng B, Jia F, Yang Y, Ying J, Zheng X-T, Bayr T, Brown JR, Capotondi A, Cobb KM, Gan B, Geng T, Ham Y-G, Jin F-F, Jo H-S, Li X, Lin X, McGregor S, Park J-H, Stein K, Yang K, Zhang L, Zhong W (2021) Changing El Niño–Southern Oscillation in a warming climate. Nat Rev Earth Env 2(9):628–644. https://doi.org/10.1038/s43017-021-00199-z

Charnock H (1955) Wind stress on a water surface. Q J R Meteorol Soc 81:639–640. https://doi.org/10.1002/qj.4970813502

Craig A, Valcke S, Coquart L (2017) Development and performance of a new version of the OASIS coupler, OASIS3-MCT_3.0. Geosci Model Dev 10:3297–3308. https://doi.org/10.5194/gmd-10-3297-2017

Curcic M, Haus BK (2020) Revised estimates of ocean surface drag in strong winds. Geophys Res Lett 47:e2020GL087647 https://doi.org/10.1029/2020GL087647

Danabasoglu G, Lamarque JF, Bacmeister J, Bailey DA, DuVivier AK, Edwards J, Emmons LKE, Fasullo J, Garcia R, Gettelman A, Hannay C, Holland MM, Large WG, Lauritzen PH, Lawrence DM, Lenaerts JTM, Lindsay K, Lipscomb WH, Mills MJ, Neale R, Oleson KW, Otto-Bliesner B, Phillips AS, Sacks W, Tilmes S, van Kampenhout L, Vertenstein M, Bertini A, Dennis J, Deser C, Fischer C, Fox-Kemper B, Kay JE, Kinnison D, Kushner PJ, Larson VE, Long MC, Mickelson S, Moore JK, Nienhouse E, Polvani L, Rasch PJ, Strand WG (2020) The community earth system model version 2 (CESM2). J Adv Model Earth Sy 12:e2019MS001916. https://doi.org/10.1029/2019MS001916

Dee DP, Uppala SM, Simmons AJ, Berrisford P, Poli P, Kobayashi S, Andrae U, Balmaseda MA, Balsamo G, Bauer P, Bechtold P, Beljaars ACM, van de Berg L, Bidlot J, Bormann N, Delsol C, Dragani R, Fuentes M, Geer AJ, Haimberger L, Healy SB, Hersbach H, Hólm EV, Isaksen L, Kållberg P, Köhler M, Matricardi M, McNally AP, Monge-Sanz BM, Morcrette J-J, Park B-K, Peubey C, de Rosnay P, Tavolato C, Thépaut J-N, Vitart F (2011) The ERA-Interim reanalysis: configuration and performance of the data assimilation system. Q J R Meteorol Soc 137:553–597. https://doi.org/10.1002/qj.828

Donelan MA, Haus BK, Reul N, Plant WJ, Stiassnie M, Graber HC, Brown OB, Saltzman ES (2004) On the limiting aerodynamic roughness of the ocean in very strong winds. Geophys Res Lett 31:L18306. https://doi.org/10.1029/2004GL019460

Drennan WM, Graber HC, Hauser D, Quentin C (2003) On the wave age dependence of wind stress over pure wind seas. J Geophys Res Oceans 108(C3):8062. https://doi.org/10.1029/2000JC000715

ECMWF (2017) IFS documentation CY47r3, Part IV: ECMWF Physical processes (ECMWF model documentation). European Centre for Medium-Range Weather Forecasts, England. http://dx.doi.org/10.21957/efyk72kl

ECMWF (2020) IFS documentation CY47r1, Part VII: ECMWF wave model (ECMWF model documentation). European Centre for Medium-Range Weather Forecasts, England. http://dx.doi.org/10.21957/31drbygag

Fairall CW, Bradley EF, Hare JE, Grachev AA, Edson JB (2003) Bulk parameterization of air–sea fluxes: updates and verification for the COARE algorithm. J Clim 16(4):571–591.

Flynn CM, Mauritsen T (2023) Hadley cell size and strength responses depend on turbulent drag. J Atmos Sci 80(4):1047–1064. https://doi.org/10.1175/JAS-D-22-0153.1

Haakenstad H, Breivik Ø, Furevik BR, Reistad M, Bohlinger P, Aarnes OJ (2021) NORA3: A nonhydrostatic high-resolution hindcast of the North Sea, the Norwegian Sea, and the Barents Sea. J Appl Meteorol Climatol 60:1443–1464. https://doi.org/10.1175/JAMC-D-21-0029.1

Hersbach H, Bell B, Berrisford P, Hirahara S, Horányi A, Muñoz-Sabater J, Nicolas J, Peubey C, Radu R, Schepers D, Simmons A, Soci C, Abdalla S, Abellan X, Balsamo G, Bechtold P, Biavati G, Bidlot J, Bonavita M, Chiara G, Dahlgren P, Dee D, Diamantakis M, Dragani R, Flemming J, Forbes R, Fuentes M, Geer A, Haimberger L, Healy S, Hogan RJ, Hólm E, Janisková M, Keeley S, Laloyaux P, Lopez P, Lupu C, Radnoti G, Rosnay P, Rozum I, Vamborg F, Villaume S, Thépaut JN (2020) The ERA5 global reanalysis. Q J R Meteorol Soc 146:1999–2049. https://doi.org/10.1002/qj.3803

Hess O, Chemke R (2024) Anthropogenic forcings reverse a simulated multi-century naturally-forced Northern Hemisphere Hadley cell intensification. Nat Commun 15:4001. https://doi.org/10.1038/s41467-024-48316-y

Holthuijsen LH, Powell MD, Pietrzak JD (2012) Wind and waves in extreme hurricanes. J Geophys Res 117:C09003. https://doi.org/10.1029/2012JC007983

Janssen PA (1989) Wave-induced stress and the drag of air flow over sea waves. J Phys Oceanogr 19:745–754.

Janssen PA (1991) Quasi-linear theory of wind-wave generation applied to wave forecasting. J Phys Oceanogr 21:1631–1642.

Janssen PA (2004) The interaction of ocean waves and wind. Cambridge University Press, Cambridge, UK. https://doi.org/10.1017/CBO9780511525018

Janssen PA, Viterbo P (1996) Ocean waves and the atmospheric climate. J Clim 9(6):1269–1287. https://doi.org/10.1175/1520-0442(1996)009%3C1269:OWATAC%3E2.0.CO;2

Janssen PA, Doyle JD, Bidlot JR, Hansen B, Isaksen L, Viterbo P (2001) Impact and feedback of ocean waves on the atmosphere. In: W. Perrie (ed) Adv Fluid Mech 33: 155–198. https://doi.org/10.21957/c1ey8zifx

Jung T, Miller MJ, Palmer TN, Towers P, Wedi N, Achuthavarier D, Adams JM, Altshuler EL, Cash BA, Kinter JL III, Marx L, Stan C, Hodges KI (2012) High-resolution global climate simulations with the ECMWF model in Project Athena: experimental design, model climate, and seasonal forecast skill. J Clim 25:3155–3172. https://doi.org/10.1175/JCLI-D-11-00265.1

Kim YH, Min SK, Son SW, Choi J (2017) Attribution of the local Hadley cell widening in the Southern Hemisphere. Geophys Res Lett 44:1015–1024. https://doi.org/10.1002/2016GL072353

Kim H, Kang SM, Kay JE, Xie S-P (2022) Subtropical clouds key to Southern Ocean teleconnections to the tropical Pacific. Proc Natl Acad Sci USA 119(34):e2200514119. https://doi.org/10.1073/pnas.2200514119

Li Q, Webb A, Fox-Kemper B, Craig A, Danabasoglu G, Large WG, Vertenstein M (2016) Langmuir mixing effects on global climate: WAVEWATCH III in CESM. Ocean Model 103:145–160. https://doi.org/10.1016/j.ocemod.2015.07.020

Li D, Staneva J, Bidlot JR, Grayek S, Zhu Y, Yin B (2021) Improving regional model skills during typhoon events: a case study for super Typhoon Lingling over the northwest Pacific Ocean. Fron Mar Sci 8:613913. https://doi.org/10.3389/fmars.2021.613913

Lohmann K, Latif M (2005) Tropical Pacific decadal variability and the subtropical–tropical cells. J Clim 18:5163–5178. https://doi.org/10.1175/JCLI3559.1

Luo J-J, Masson S, Roeckner E, Madec G, Yamagata T (2005) Reducing climatology bias in an ocean–atmosphere CGCM with improved coupling physics. J Clim 18:2344–2360. https://doi.org/10.1175/JCLI3404.1

Madec G, and the NEMO System Team (2022) NEMO ocean engine reference manual (v4.2.0). In: Scientific Notes of IPSL Climate Modelling Center. Zenodo. https://doi.org/10.5281/zenodo.6334656

Matthes K, Biastoch A, Wahl S, Harlaß J, Martin T, Brücher T, Drews A, Ehlert D, Getzlaff K, Krüger F, Rath W, Scheinert M, Schwarzkopf FU, Bayr T, Schmidt H, Park W (2020) The Flexible Ocean and Climate Infrastructure version 1 (FOCI1): mean state and variability. Geosci Model Dev 13(6):2533–2568. https://doi.org/10.5194/gmd-13-2533-2020

Miller MJ, Beljaars ACM, Palmer TN (1992) The sensitivity of the ECMWF model to the parameterization of evaporation from the tropical oceans. J Clim 5(5):418–434.

Nguyen H, Evans A, Lucas C, Smith I, Timbal B (2013) The Hadley circulation in reanalyses: climatology, variability, and change. J Clim 26:3357–3376. https://doi.org/10.1175/JCLI-D-12-00224.1

Pineau-Guillou L, Bouin MN, Ardhuin F, Lyard F, Bidlot JR, Chapron B (2020) Impact of wave-dependent stress on storm surge simulations in the North Sea: Ocean model evaluation against in situ and satellite observations. Ocean Model 154:101694. https://doi.org/10.1016/j.ocemod.2020.101694

Powell MD, Vickery PJ, Reinhold TA (2003) Reduced drag coefficient for high wind speeds in tropical cyclones. Nat 422:279–283. https://doi.org/10.1038/nature01481

Qiao F, Yuan Y, Yang Y, Zheng Q, Xia C, Ma J (2004) Wave-induced mixing in the upper ocean: distribution and application to a global ocean circulation model. Geophys Res Lett 31:L11303. https://doi.org/10.1029/2004GL019824

Qiao F, Yuan Y, Ezer T, Xia C, Yang Y, Lü X, Song Z (2010) A three-dimensional surface wave–ocean circulation coupled model and its initial testing. Ocean Dynam 60:1339–1355. https://doi.org/10.1007/s10236-010-0326-y

Rayner NA, Parker DE, Horton EB, Folland CK, Alexander LV, Rowell DP, Kent EC, Kaplan A (2003) Global analyses of sea surface temperature, sea ice, and night marine air temperature since the late nineteenth century. J Geophys Res-Atmos 108:4407. https://doi.org/10.1029/2002JD002670

Roberts MJ, Baker A, Blockley EW, Calvert D, Coward A, Hewitt HT, Jackson LC, Kuhlbrodt T, Mathiot P, Roberts CD, Schiemann R, Seddon J, Vannière B, Vidale PL (2019) Description of the resolution hierarchy of the global coupled HadGEM3-GC3. 1 model as used in CMIP6 HighResMIP experiments. Geosci Model Dev 12:4999–5028. https://doi.org/10.5194/gmd-12-4999-2019

Savita A, Kjellsson J, Kedzierski RP, Latif M, Rahm T, Wahl S, Park W (2024) Assessment of climate biases in OpenIFS version 43r3 across model horizontal resolutions and time steps. Geosci Model Dev 17:1813–1829. https://doi.org/10.5194/gmd-17-1813-2024

Shimura T, Mori N, Takemi T, Mizuta R (2017) Long-term impacts of ocean wave-dependent roughness on global climate systems. J Geophys Res-Oceans 122:1995–2011. https://doi.org/10.1002/2016JC012621

Sieker T, Kjellsson J, Park W (2026) Impact of ocean resolution on the North Atlantic bias in the FOCI-OpenIFS climate model. Climate Dynamics, (in press).&#12601

Song Z, Qiao F, Song Y (2012) Response of the equatorial basin-wide SST to non-breaking surface wave-induced mixing in a climate model: an amendment to tropical bias. J Geophys Res Oceans. https://doi.org/10.1029/2012JC007931

Su J, Zhang R, Rong X, Min Q, Zhu C (2018) Sea surface temperature in the subtropical Pacific boosted the 2015 El Niño and hindered the 2016 La Niña. J Clim 31(2):877–893. https://doi.org/10.1175/JCLI-D-17-0379.1

Sun B (2018) Asymmetric variations in the tropical ascending branches of Hadley circulations and the associated mechanisms and effects. Adv Atmos Sci 35:317–333. https://doi.org/10.1007/s00376-017-7089-z

Takaya Y, Bidlot JR, Beljaars AC, Janssen PA (2010) Refinements to a prognostic scheme of skin sea surface temperature. J Geophys Res Oceans 115(C6):C06009. https://doi.org/10.1029/2009JC005985

Taylor PK, Yelland MJ (2001) The dependence of sea surface roughness on the height and steepness of the waves. J Phys Oceanogr 31(2):572–590.

Tian B, Dong X (2020) The double-ITCZ bias in CMIP3, CMIP5, and CMIP6 models based on annual mean precipitation. Geophys Res Lett 47(8):e2020GL087232 https://doi.org/10.1029/2020GL087232

Wang C, Hu Y, Wen X, Zhou C, Liu J (2020) Inter-model spread of the climatological annual mean Hadley circulation and its relationship with the double ITCZ bias in CMIP5. Clim Dyn 55(9):2823–2834. https://doi.org/10.1007/s00382-020-05414-z

Webb DJ, de Cuevas BA (2007) On the fast response of the Southern Ocean to changes in the zonal wind. Ocean Sci 3(3):417–427. https://doi.org/10.5194/os-3-417-2007

Wu J (1980) Wind-stress coefficients over sea surface near neutral conditions: a revisit. J Phys Oceanogr 10(5):727–740.

Yao B, Teng S, Lai R, Xu X, Yin Y, Shi C, Liu C (2020) Can atmospheric reanalyses (CRA and ERA5) represent cloud spatiotemporal characteristics? Atmos Res 244:105091. https://doi.org/10.1016/j.atmosres.2020.105091

Zuidema P, Chang P, Medeiros B, Kirtman BP, Mechoso R, Schneider EK, Toniazzo T, Richter I, Small RJ, Bellomo K, Brandt P, de Szoeke S, Farrar JT, Jung E, Kato S, Li M, Patricola-Dirosario C, Wang Z, Wood R, Xu Z (2016) Challenges and prospects for reducing coupled climate model SST biases in the eastern tropical Atlantic and Pacific oceans: the US CLIVAR Eastern Tropical Oceans Synthesis Working Group. Bull Am Meteorol Soc 97(12):2305–2328. https://doi.org/10.1175/BAMS-D-15-00274.1

Zuo H, Balmaseda MA, Tietsche S, Mogensen K, Mayer M (2019) The ECMWF operational ensemble reanalysis–analysis system for ocean and sea ice: a description of the system and assessment. Ocean Sci 15:779–808. https://doi.org/10.5194/os-15-779-2019

Publisher's note Springer Nature remains neutral with regard to jurisdictional claims in published maps and institutional affiliations.

Springer Nature or its licensor (e.g. a society or other partner) holds exclusive rights to this article under a publishing agreement with the author(s) or other rightsholder(s); author self-archiving of the accepted manuscript version of this article is solely governed by the terms of such publishing agreement and applicable law.